

# Ionospheric Calibration of Low Frequency Radio Interferometric Observations using the Peeling Scheme

## II. Method Extensions & Application to a Larger Array

H.T. Intema<sup>1</sup>, S. van der Tol<sup>2</sup>, W.D. Cotton<sup>3</sup>, A.S. Cohen<sup>4</sup>, I.M. van Bemmelen<sup>1</sup>, and H.J.A. Röttgering<sup>1</sup>

<sup>1</sup> Leiden Observatory, Leiden University, P.O.Box 9513, NL-2300 RA, Leiden, The Netherlands

<sup>2</sup> Electr. Engineering, Math. and Computer Science, Delft University of Technology, Delft, The Netherlands

<sup>3</sup> National Radio Astronomy Observatory, Charlottesville, VA, USA

<sup>4</sup> Naval Research Laboratory, Washington DC, USA

Received ... / Accepted ...

### Abstract

In a previous article, we presented a description and first results of SPAM (Source Peeling and Atmospheric Modeling), a method for calibration of direction-dependent ionospheric phase errors in low-frequency radio interferometric observations. By assuming a time-constant instrumental phase offset per antenna, and by representing the ionosphere with a single 2-dimensional phase screen model at fixed height, SPAM was able to improve the calibration accuracy of 74 MHz observations from the VLA in relatively compact configurations ( $\lesssim 20$  km baselines) as compared to other existing calibration methods. In this paper, we present two extensions of the SPAM method: a multi-layer ionosphere model to represent vertical ionospheric structure, and an estimator for slow instrumental phase drifts in the presence of ionospheric phase fluctuations. We describe the data reduction steps while applying SPAM on archival 74 MHz observational data from the Very Large Array in its most extended A-configuration (up to 35 km baselines) during quiet ionospheric conditions. Detection and removal of phase drifts significantly reduces the RMS residual phase when fitting ionospheric phase models. The two target field data sets are calibrated and imaged using both the single-layer and multi-layer ionosphere model. Image analysis shows an equal performance of the single- and multi-layer models in terms of background noise ( $\sim 30$  mJy beam<sup>-1</sup>) and source peak fluxes, but a slight (5–10 percent) improvement in the overall astrometric accuracy of the multi-layer model images. This outcome is consistent with the concept of a smooth bulk ionosphere that is poorly represented by a single-layer model.

**Key words.** Atmospheric effects – Methods: numerical – Techniques: interferometric

### 1. Introduction

For ground-based radio interferometry at low frequencies ( $\lesssim 300$  MHz), the Earth's ionosphere is one of the main sources of error in phase (e.g., Thompson, Moran & Swenson 2001). The partially ionized gas (mainly the free electrons), permeated with the Earth's magnetic field, causes refraction and propagation delay to passing radio waves. Because the ionosphere is dynamic and inhomogeneous, the refractive index for radio waves changes with position and time. This influences the ray path of the radio wave and the amount of ionospheric phase rotation accumulated along the ray path. The phase rotation scales (approximately) linearly with frequency and with free electron column density (total electron content, or TEC) along the ray path. The presence of the magnetic field adds complexity by introducing Faraday rotation, a differential phase rotation between left- and right-polarized waves (which is not considered further in this article).

An interferometer array measures phase differences to determine the direction of incident radio waves. The ionosphere adds a differential phase rotation to the complex-

valued visibility measurement on each baseline, which is the difference of the phase rotation along two lines-of-sight (LoSs) from the two baseline antennas towards the cosmic radio source. Under *non-isoplanatic* conditions, the differential phase error on a single baseline varies with source position in the field-of-view (FoV). This is typically the case for wide-field, low-frequency observations. Calibration of the visibility measurements requires direction-dependent, antenna-based phase corrections. Calibration methods that yield direction-independent phase corrections (like self-calibration; e.g., see Pearson & Readhead 1984) will therefore not work. For optimal performance of existing and future low-frequency radio interferometer arrays (e.g., VLA, GMRT, LOFAR, LWA and SKA), it is crucial to have calibration algorithms available that can properly model and remove direction-dependent ionospheric phase contributions from the visibilities.

There are currently two existing calibration methods for radio interferometers that incorporate direction-dependent ionospheric phase errors: *field-based calibration* (FBC) by Cotton et al. (2004) and *source peeling & atmospheric modeling* (SPAM) by Intema et al. (2009). Both methods attempt to separate ionospheric from instrumental phase errors on the basis of temporal and spatial behaviour. The

---

Send offprint requests to: H.T. Intema,  
e-mail: intema@strw.leidenuniv.nl

instrumental phase error per antenna is assumed to be approximately constant with time and viewing direction. The direction-dependent ionospheric phase rotation is modeled with a phase screen over the array.

FBC has been designed and used extensively for calibration of relatively compact arrays, mainly the 74 MHz VLA (Kassim et al. 2007) in B-configuration ( $\lesssim 11$  km; e.g., Cohen et al. 2007). FBC assumes that the instantaneous differential ionospheric phase structure over the array in any viewing direction can be accurately described by a gradient, and that this gradient varies smoothly with viewing direction (the physical nature of the ionosphere imposes some form of continuity on the ionospheric phase structure across the FoV of each antenna). Effectively, the 3-dimensional structure of the ionosphere is integrated along an average LoS from the array into a 2-dimensional phase gradient screen at infinite height. The performance of FBC degrades in the presence of higher-order phase structure over the array.

The relatively new SPAM method attempts to correct for higher order phase structure over the array. Assuming that the dominant phase errors originate from a limited height range in the ionosphere, SPAM attempts to combine the observed instantaneous direction-dependent, higher order ionospheric phase structure over the array into a thin-layer phase model at some representative height. By using an airmass function to incorporate a zenith angle dependence, the thin-layer phase model is in effect again reduced to 2 spatial dimensions.

In this article, we attempt to relax two potentially limiting assumptions of the current SPAM algorithm: the thin ionospheric layer and the stable instrumental phase. In Section 2 we discuss the limitations of a thin-layer ionosphere model. In Section 3, we present a detailed description of a multi-layer extension of the ionospheric model in SPAM, as well as a method for estimating slow instrumental phase drifts. In Section 4, we present the results of SPAM calibration on VLA 74 MHz observations in the largest A-configuration, using both single- and multi-layer ionosphere models, and compare the results. A discussion and conclusions are presented in Section 5.

## 2. Representations of the 3-dimensional Ionosphere

In this Section, we describe some of the basic steps in ionospheric modeling, estimate the first-order phase error from using a single thin-layer model, and provide a background for construction of a multi-layer model.

### 2.1. Ionospheric Phase Rotation

The ionosphere (e.g., Davies 1990) is a thick shell of partially ionized gas, extending roughly from  $\sim 50$  km height into outer space ( $> 1000$  km). The free electron density, most relevant for our problem, varies with time and location, influenced mainly by the Sun (direct photoionization through radiation, particle injection through the solar wind). On average, the electron density peaks at 300–400 km height.

A radio wave with frequency  $\nu$  that travels from an extraterrestrial source  $k$  towards a ground-based antenna  $i$  experiences a propagation delay, and therefore a phase rotation  $\phi_{ik}$ , due to free electrons with density  $n_e$  along its path

through the ionosphere. By assuming the ionosphere is an unmagnetized, cold, collisionless plasma and the observing frequency  $\nu$  is much larger than the plasma frequency (typically 1–10 MHz), the ionospheric phase rotation is given by

$$\phi_{ik} = \frac{e^2}{4\pi\epsilon_0 m c \nu} \int_k^i n_e dl, \quad (1)$$

with  $e$  the electron charge,  $\epsilon_0$  the vacuum permittivity,  $m$  the electron mass,  $c$  the speed of light in vacuum. The integral on the right is the column density of free electrons along the line-of-sight (LoS), commonly known as total electron content (TEC). Measuring phase rotations on radio signals is a powerful tool to study the ionosphere. Ionospheric researchers distinguish between vertical TEC (VTEC) along a vertical LoS, and slant TEC (STEC) along a LoS at a non-zero zenith angle. The related TEC unit (TECU) is  $10^{16} \text{ m}^{-2}$ , a typical value for the VTEC during nighttime. In daytime, the VTEC may locally increase with 1–2 orders of magnitude.

On smaller scales, the coupling with acoustic-gravity waves in the troposphere is known to generate wave-like horizontally traveling ionospheric disturbances (TIDs) at 200–400 km height, with wavelengths between 200–500 km, traveling at speeds of 300–700 km h<sup>-1</sup> in any direction, giving rise to 1–5 percent changes in VTEC. Fluctuations on even smaller scales are less well understood, but are known to give rise to scintillations in astronomical radio observations. These  $\sim 0.1$  percent fluctuations in TEC appear to originate from a turbulent layer roughly 100 km below the peak in the electron density (van Velthoven 1990).

A radio interferometer (or array) correlates the radio signals received from cosmic sources on pairs of antennas (baselines) into complex visibility measurements, which are approximate spatial Fourier components of the apparent sky brightness distribution (e.g., Thompson, Moran & Swenson 2001). The ionospheric phase error in the visibility contribution of a source  $k$ , measured on antennas  $i$  and  $j$ , is the differential phase rotation along the LoS from  $k$  to  $i$  and the LoS from  $k$  to  $j$ :

$$\phi_{ijk} = \phi_{ik} - \phi_{jk} \quad (2)$$

For a given viewing direction, the array is most sensitive to differential ionospheric phase structure on horizontal spatial scales comparable or smaller than the array. Large-scale changes (e.g., during sunrise/sunset) in the ionospheric free electron density can cause steep phase gradients to appear over the array in all directions, but these gradual changes are generally easy to track and remove.

### 2.2. Ionosphere Models

Despite the true 3-dimensional structure of the ionosphere, 2-dimensional models with a screen at a fixed, representative height above the earth's surface have been used extensively to characterize the ionosphere. VTEC screen models are used for ionospheric research and for radio navigation applications (e.g., see Smith et al. 2008). The VTEC is most often derived from ground-based slant TEC measurements (STEC, measured at non-zero zenith angle) with the ionosphere being back-lighted by some radio source, e.g. a satellite. Two-dimensional screens are mathematically simple, computationally cheap and can be constructed with

relatively few measurements. Smith et al. estimate that under normal ionospheric conditions (i.e. no solar activity and away from the Sun-induced ionized bubble over the geomagnetic equator) the RMS VTEC accuracy of 2-dimensional screens is at best 1 TECU. For dense networks of GPS receivers, the local differential TEC accuracy can be a factor of 10–100 better (REFERENCE NEEDED).

Tomographic reconstruction of the 3-dimensional electron density structure from TEC measurements is more difficult but possible (see Bust & Mitchell 2008 for an overview) if sufficient STEC measurements through the volume of interest are available for a variety of viewing angles. This yields more accurate VTEC estimates ( $\lesssim 1$  TECU) at the cost of adding complexity to the model. Global 3-dimensional models for the ionosphere are publicly available (e.g., the International Reference Ionosphere; Bilitza 2001). Typically, in the absence of a dense constellation of satellites and ground-based receivers, the spatial resolution of 3-dimensional ionosphere models is in the order of 50–100 km at best.

Current low-frequency radio arrays (e.g., VLA and GMRT) are not equipped with dedicated (GPS) systems to measure the local ionosphere over the array. Also, the currently best achievable accuracy would not be sufficient to directly calibrate the instrument, but could provide a starting point for further calibration actions. For a VLA observation at 74 MHz, a differential TEC accuracy of 0.01 TECU is equivalent to an ionospheric phase rotation of  $\sim 1$  radian. The global models are generally too coarse in accuracy and spatial and temporal resolution to be of use for calibration.

For high accuracy calibration on small spatial scales, a radio array relies on direct calibration against cosmic radio sources to derive an accurate model for ionospheric phase rotations. Under the assumption that the small-scale phase fluctuations originate from a thin layer below the electron density peak, SPAM calibration contains a 2-dimensional phase screen model that has been placed at 200 km height during successful initial testing (Intema et al. 2009). The RMS residual phase after model fitting is 20 – 25 degrees at 74 MHz, which includes the propagated error from the data acquisition. This corresponds to a differential TEC accuracy of  $3.5 \times 10^{-3}$  TECU. The SPAM model yields no information on absolute TEC.

The 2-dimensional SPAM model (SPAM2D from here on) mimicks the integrated phase effect from a thin, turbulent layer of free electrons, much thinner than the scale size of dominant electron density fluctuations in the ionosphere. The model is a function of both the horizontal ionospheric pierce point (IPP) coordinate  $\mathbf{p}$  and the local zenith angle  $\zeta$  under which the straight LoSs from an antenna towards a source pierces through the layer:

$$\phi(\mathbf{p}, \zeta) = \frac{\phi(\mathbf{p})}{\cos(\zeta)}. \quad (3)$$

For a given antenna position, source position and layer height,  $\mathbf{p}$  and  $\zeta$  are fully determined (see Figure 2 in Intema et al. 2009). The function  $\phi(\mathbf{p})$  describes the stochastic horizontal phase structure, expressible in terms of an isotropic phase covariance function (see Section 3.1). The airmass term  $1/\cos(\zeta)$  extends the horizontal phase structure over some limited vertical range. Equation 3 is combined with Equation 2 to produce model phase differences. The free model parameters contained within  $\phi(\mathbf{p})$  are determined per integration interval by non-linear least squares (NLLS)

fitting of the model phase differences against estimates of the differential ionospheric phase errors in several viewing directions. The latter estimates are derived from individual phase calibrations on available calibrator sources in the field-of-view (FoV), a technique known as *peeling* (Noordam 2004).

### 2.3. First Order Bulk Ionosphere Error

By including only a limited height range in the SPAM2D model, we have ignored the effect of the ionosphere outside this height range. Here we estimate the magnitude of the phase errors that may arise when using a 2-dimensional phase screen model to model the instantaneous 3-dimensional bulk ionosphere. For convenience, we ignore the  $2\pi$  phase ambiguities that are inherent in the visibility measurements by a radio interferometer.

We define the bulk ionosphere as a smooth spatial electron density distribution that varies on spatial scales that are much larger than the array we aim to calibrate. We assume that any differences observed in the bulk TEC along parallel LoSs are dominated by geometric differences rather than intrinsic differences. Using several simplifying assumptions, we estimate the order of magnitude of the phase error introduced by this incompleteness under normal ionospheric conditions.

For the discussion here, the total ionospheric electron content is assumed to consist only of the bulk and a thin turbulent layer. We further assume that the resulting differential phase rotation towards calibrator sources can be accurately measured with the array through peeling. Finally, we assume that the SPAM2D model is accurate in reproducing and interpolating the phase contribution originating from the turbulent layer. Because ionospheric phase rotation is linear in TEC, and the SPAM2D model is linear in its free parameters, the modeling of the total ionosphere can be separated into a bulk part and a turbulent layer part. In the following, we focus on the bulk part only.

Smith et al. (2008) evaluated the reconstruction accuracy of VTEC from STEC measurements through the use of a 2-dimensional shell for modeling the ionosphere. Based on ray-tracing through the 3-dimensional US-TEC ionosphere model (Fuller-Rowell 2006), they derived an empirical mapping function for 2-dimensional screens that significantly improves the conversion from STEC to VTEC as compared to the  $1/\cos(\zeta)$  airmass function. Our application differs from theirs in that we aim to solve for *differential* ionospheric phase rotation along the two LoSs for each baseline rather than solving for absolute TEC along a single LoS. For estimation of the first order error due to the bulk ionosphere, we make use of their improved mapping function:

$$\text{STEC} = \frac{\text{VTEC}}{[1 - f] \cos(\zeta)}. \quad (4)$$

The empirical function  $f$  depends on both the chosen screen height  $h$  and the zenith angle  $\zeta$  at the IPP, and is given by

$$\begin{aligned} f &= (a + b h) \\ a &= a_3(a_2 + \tan^{-1}(a_1(\zeta + a_0))) \\ b &= b_3(b_2 + \tan^{-1}(b_1(\zeta + b_0))), \end{aligned} \quad (5)$$

with the fitted values for the parameters  $a_x$  and  $b_x$  given in Table 1. The valid zenith angle domain runs approxi-

$x$	$a_x$	$b_x$
0	-64.4297	-64.3659
1	0.0942437	0.104974
2	1.39436	1.41152
3	-0.196357	0.000463341

Table 1: Fitted values for the empirical function in Equation 5, with  $h$  in km and  $\zeta$  in degrees.

mately from 0–65 degrees. According to Smith et al., this mapping function is 30–50 percent more accurate than using  $1/\cos(\zeta)$  for estimating absolute VTEC measurements. We anticipate that the differential accuracy is even more accurate, but to be conservative we may need to multiply the errors derived below with a factor of 2–3.

The observable (differential) ionospheric phase rotation  $\phi_{ijk}^b$  due to the bulk on a baseline consisting of antennas  $i$  and  $j$ , looking towards source  $k$  (see Figure 1) is given by (Equation 2):

$$\phi_{ijk}^b = \phi_{ik}^b - \phi_{jk}^b. \quad (6)$$

For the ionospheric volume of interest, we assume that the VTEC is approximately constant. Due to the linear relation between TEC and phase rotation (Equation 1), we can rewrite Equation 4 in terms of phase:

$$\phi_{ik}^b = \frac{\phi_v^b}{[1 - f_{ik}] \cos(\zeta_{ik})}, \quad (7)$$

with  $\phi_v^b$  the constant bulk phase rotation along a vertical LoS.

We assume that the SPAM2D model (Equation 3) can be accurately fitted to the collection of *measured* phase differences  $\{\phi_{ijk}^b\}$ :

$$\phi_{ijk}^b = \frac{\phi^b(\mathbf{p}_{ik})}{\cos(\zeta_{ik})} - \frac{\phi^b(\mathbf{p}_{jk})}{\cos(\zeta_{jk})}. \quad (8)$$

We now consider two LoSs from a different baseline, consisting of antennas  $i' \neq i$  and  $j' \neq j$  looking towards source  $k' \neq k$ , that pierce the screen model at the same IPPs but under different zenith angles:

$$\mathbf{p}_{i'k'} = \mathbf{p}_{ik}, \quad \mathbf{p}_{j'k'} = \mathbf{p}_{jk}, \quad \zeta_{i'k'} \neq \zeta_{ik}, \quad \zeta_{j'k'} \neq \zeta_{jk} \quad (9)$$

The bulk ionospheric phase rotation  $\phi_{i'j'k'}^b$  for this baseline is given by:

$$\phi_{i'j'k'}^b = \phi_{i'k'}^b - \phi_{j'k'}^b \quad (10)$$

Based on our previous fit (Equation 8), the predicted phase rotation for this baseline is

$$\hat{\phi}_{i'j'k'}^b = \frac{\phi^b(\mathbf{p}_{ik})}{\cos(\zeta_{i'k'})} - \frac{\phi^b(\mathbf{p}_{jk})}{\cos(\zeta_{j'k'})}, \quad (11)$$

where we have used Equation 9. The absolute error in this prediction is defined by

$$\Delta \phi_{i'j'k'}^b = |\hat{\phi}_{i'j'k'}^b - \phi_{i'j'k'}^b| \quad (12)$$

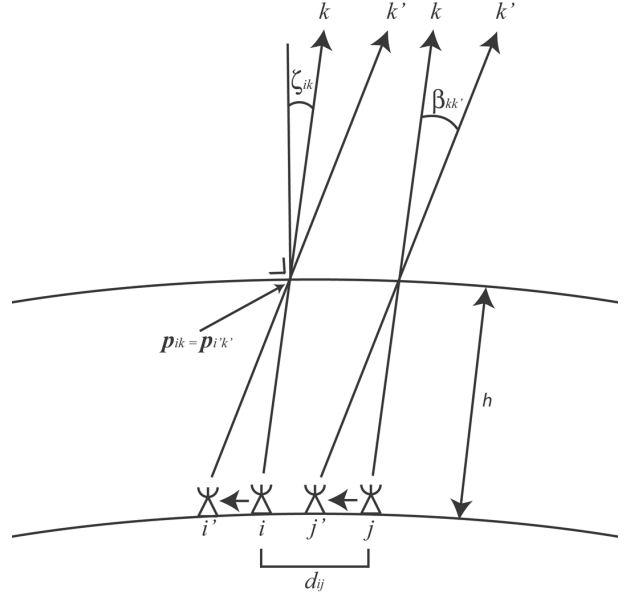


Figure 1: Schematic overview of the calibration geometry used for estimating the phase error in the SPAM2D single-layer model from ignoring the bulk ionosphere. Two antennas  $i$  and  $j$ , at distance  $d_{ij}$  from each other, form a baseline  $ij$  that observes calibrator source  $k$ . The SPAM2D model, consisting of a single-layer model at height  $h$ , is fitted to the measurable differential (bulk) ionospheric phase rotations at the IPPs  $\{\mathbf{p}\}$ , assuming a  $1/\cos(\zeta)$  airmass dependence. For a second baseline  $i'j'$  observing a source  $k'$  at angular distance  $\beta_{kk'}$  from source  $k$ , sharing the same IPPs, the SPAM2D model is used to predict the differential phase rotation for this baseline. For a bulk ionosphere with constant VTEC, the prediction will differ from the real differential phase rotation, because the true airmass dependence is more complex than  $1/\cos(\zeta)$ .

Because the fitting to differential phase (Equation 10) allows for an arbitrary offset to be added to the model, we assume a zero mean phase for the model near the pierce points. For simplicity, we only consider the scenario in Figure 1 where all antennas  $i, j, i', j'$  lie on the intersection line of the Earth's surface and a plane through sources  $k, k'$  and the center of the Earth. The distance between antennas  $i$  and  $i'$  (or  $j$  and  $j'$ ) is related with the angular separation  $\beta_{kk'}$  between sources  $k$  and  $k'$ . The maximum possible value of  $\beta_{kk'}$  is either determined by the size of the FoV or the size of the array. For the VLA at 74 MHz in A-configuration, the FoV is roughly as large as the angular size of the array as seen from a screen height of 200 km (both  $\sim 10$  degrees). In practise,  $\beta_{kk'}$  will be smaller than this, because a typical FoV contains multiple calibrator sources  $\{k\}$  and because both antennas of a shifted baseline are bound to the array dimensions.

For the 74 MHz VLA in A-configuration, we have calculated the absolute error in the phase prediction by a single-layer model at 300 km height for a number of different situations. For the default SPAM2D height of 200 km, the mapping function in Equations 4 and 5 appears to be less accurate for large ( $\gtrsim 55$  degrees) zenith angles. We found that our error estimates change very little with screen height,

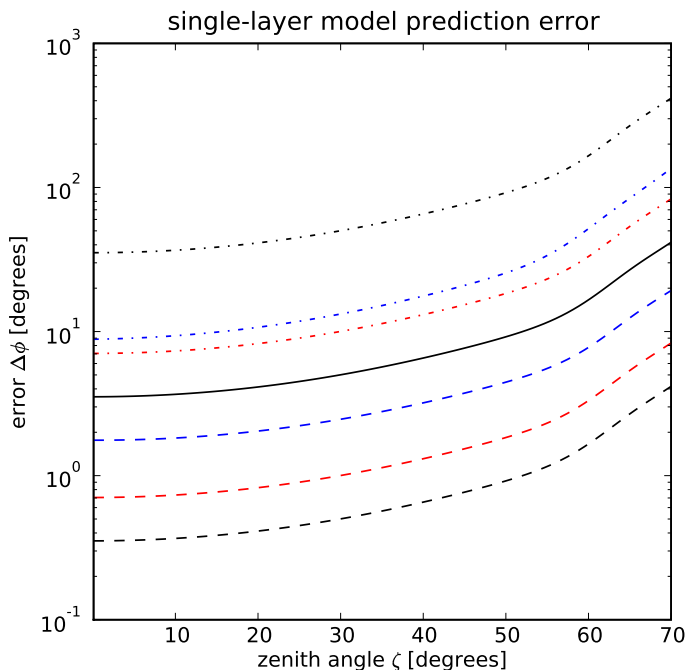


Figure 2: Plots of the estimated error  $\Delta\phi$  in the prediction of an ideal single-layer ionosphere model in the presence of a bulk ionosphere with constant VTEC. These plots are derived for the 74 MHz VLA in A-configuration and a layer height of 300 km. For a baseline of 10 km and an angular separation of 2 degrees, the error is plotted as a function of zenith angle for VTEC values of 1, 10 and 100 TECU (dashed, solid and dotted black lines, respectively). Also, for a VTEC value of 10 TECU and an angular separation of 2 and 20 km (dashed and dotted red lines, respectively). Furthermore, for a VTEC value of 10 TECU and a baseline length of 10 km, the error is plotted for angular separations of 1 and 5 degrees (dashed and dotted blue lines, respectively). Note that the zenith angle used here is the (mean) zenith angle at the antennas, from which the zenith angles at the IPPs is derived.

therefore we use 300 km instead. In Figure 2 the error is plotted as a function of zenith angle for different possible values of VTEC, baseline length and angular separation. Except for larger zenith angles ( $\gtrsim 60$  degrees) or the sporadic case of an extremely large VTEC value ( $\sim 100$  TECU) during an ionospheric storm, all error values are in the order of 30 degrees or less. To incorporate possible inaccuracies in the mapping function, this may need to be multiplied by a factor of 2–3, which may raise the error to significant proportions.

Apart from the anticipated linear relation between error and both VTEC and wavelength, there also exists an approximate linear relation between the error and both baseline length and angular separation over the parameter domains investigated here. The linear relation between error and baseline length causes a phase gradient over the array, which results in an apparent position shift of source  $k'$ . This may be one of the causes of the systematic source position offsets that were observed by Intema et al. 2009 in image regions without calibrators.

## 2.4. Multi-layer Models

The error estimates from the previous Section show that even under the most ideal ionospheric conditions, the use of a 2-dimensional phase screen can lead to significant prediction errors. In the additional presence of irregular vertical electron density variations, the 2-dimensional representation will degrade further. This argues for the use of a 3-dimensional model for ionospheric calibration instead, but this transition is not straightforward.

The SPAM2D phase screen is designed to have certain properties to aid model fit convergence and interpolation: (i) the model base vectors are orthogonal on the discrete IPP domain, (ii) model order reduction leads to minimal deviation from the assumed statistical behaviour, (iii) interpolation retains the assumed statistical behaviour, (iv) the model has most spatial structure near the IPPs and converges to zero at large distance. For the construction of a 3-dimensional model, it is highly desirable to maintain these characteristics while adding more freedom to the model to represent the vertical structure.

The problem of astronomical imaging in the presence of atmospheric turbulence has been addressed for many years in optical and near-infrared astronomy. To overcome the typical optical *seeing* resolution limit of  $\sim 1''$  due to tropospheric turbulence, large ground-based telescopes have been equipped with adaptive optics systems (AO; e.g., Hardy 1998) that track the atmospheric distortion of a (possibly artificial laser) guide star in the target field, and change the shape of a deformable mirror in real-time to correct the distorted wavefronts. This generally leads to significant improvements in image resolution near the guide star, but performance decreases at larger distance. The development of telescopes with increasing fields-of-view ( $\gtrsim 10'$ ) also triggered the development of multi-conjugate adaptive optics (MCAO; e.g., Esposito 2005). This technique uses multiple guide stars to allow for significant wavefront corrections over a larger sky area, using multiple deformable mirrors to represent turbulent layers at different (conjugate) heights in the troposphere. This technique has been successfully tested on several selected fields (Marchetti 2007).

The concept of dividing the vertical dimension of a distorting atmospheric volume into a number of representative layers has also been proposed for ionospheric modeling. Airplane navigation in the United States is aided by the Wide Area Augmentation System (WAAS), which includes a thin-layer ionosphere model for correcting propagation delays in GPS-signals. Blanch et al. (2004) propose a generalization of the ionosphere model by introducing multiple (statistically independent) thin layers at representative heights. The total propagation delay for any (straight) LoS from GPS satellite to receiver is assumed to be the sum of the contributions of the individual layers. In effect, the TEC integral (Equation 1) along the LoS through the ionosphere is replaced by a simpler sum. For two test cases on real data, the multi-layer ionosphere model reduces the VTEC estimation error by 30–50 percent as compared to the single-layer model.

Due to the similarities in model setup, we can apply the multi-layer approach of Blanch et al. to the SPAM model. The introduction of multiple but similar turbulent layers does not change the statistics of phase rotations detected at ground level as (Roddier 1981). This approach meets

our requirement to maintain the important properties of the SPAM2D model mentioned above while adding more freedom to the model to represent the vertical structure. An important additional property is that there is no redundancy between model layers. Details of the implementation are described in Section 3.1.

### 3. Method

In this Section we describe two extensions of the SPAM ionospheric calibration method, namely the multi-layer ionospheric model and the estimator for slow instrumental phase drifts. Both these extensions are aimed at achieving high phase calibration accuracy over the whole FoV during extended radio interferometer observing runs at low frequencies. Because the original SPAM method is described extensively in Intema et al. 2009, we repeat here only those parts of the method that are relevant for defining the extensions.

#### 3.1. Ionospheric Multi-layer Phase Screen Model

In the previous version of SPAM, the ionosphere is represented by a single curved phase screen, modeling a thin turbulent layer, at a fixed height  $h$  above the Earth's surface. The accuracy of this model degrades in the presence of significant variation in the vertical electron density structure. Under these conditions, the ionosphere must be represented by a model that includes a more extended form of height-dependence than an airmass term.

SPAM has been extended with a multi-layer ionospheric phase model that allows for multiple independent phase screens to be positioned at representative heights  $\{h\}$ . In the multi-layer model, individual phase screens are defined in (nearly) the same way as for the single-layer model in Intema et al. (2009; Section 3.4 and Appendix A). Each layer represents a thin layer of (zero mean) turbulent electron density fluctuations, expressible in terms of an isotropic phase covariance function. For a single visibility time interval (we omit the time subscript  $n$  here), the total (integrated) ionospheric phase delay for a radio wave traveling along a given *straight* line-of-sight (LoS) from antenna  $i$  to source  $k$  is modeled by a weighted sum of phase delays induced by piercing through the individual phase screens:

$$\phi_{ik} = \sum_h w_h \phi_{ik}^h = \sum_h w_h \frac{\phi^h(\mathbf{p}_{ik}^h)}{\cos(\zeta_{ik}^h)}, \quad (13)$$

where  $w_h$  is the weight assigned to each layer (with  $\sum_h w_h = 1$ ),  $\mathbf{p}_{ik}^h$  the coordinates of the point where the LoS pierces through the phase screen at height  $h$ , and  $\zeta_{ik}^h$  the zenith angle of the LoS at the pierce point. For a finite set of LoSs of different antenna-source pairs  $\{(i, k)\}$ , the phase contributions of one layer can be described by a phase vector  $\Phi^h = [\dots \phi^h(\mathbf{p}_{ik}^h) \dots]^T$ . Following Equation 13, the total phase vector  $\Phi$  is a linear combination of the layer-based phase vectors:

$$\Phi = \sum_h w_h \mathbf{A}^h \Phi^h, \quad (14)$$

with  $\mathbf{A}^h$  a diagonal matrix with the  $1/\cos(\zeta_{ik}^h)$  airmass terms on the diagonal.

For the original single-layer model, an optimal set of orthogonal base vectors to describe the phase screen were derived by performing a discrete Karhunen-Loève (KL) transform on the values of the phase covariance function between pairs from a set of IPPs, which are located on the phase screen along the LoSs from the observing antennas towards several bright calibrator sources in the field-of-view (FoV). The base vector coefficients (the free model parameters) were derived by a non-linear least-squares (NLLS) fit of the phase screen model to the calibration phase solutions that were obtained by peeling the bright calibrator sources. Interpolation of the phase screen away from the IPPs is done through Kriging interpolation (Matheron 1973). For details we refer to Intema et al. (2009) and references therein.

Construction of the multi-layer model is done in a similar way. After determining the covariance function between pairs of IPPs in individual layers, the total phase covariance between pairs of LoSs is calculated by a weighted sum of the phase covariances from the individual layers (Blanch et al. 2004). Performing a KL transform on the total phase covariances now yields an optimal set of orthogonal base vectors for describing the vertically integrated phase effect of the full turbulent multi-layer model. Details on how to derive the base vectors and how to interpolate them for arbitrary LoSs follow below. This approach has two desirable properties: (i) each base vector coefficient (or free model parameter) applies to all layers simultaneously and does not have to be arbitrarily assigned to a single layer, and (ii) the base vectors are orthogonal over the integrated vertical model structure, therefore there is (intrinsically) no redundancy between model layers.

Following van der Tol & van der Veen (2007), the stochastic model for each layer is defined in terms of a power-law phase structure function

$$D_{\phi\phi}^h(r) = \langle [\phi^h(\mathbf{p}^h) - \phi^h(\mathbf{p}^h + \mathbf{r})]^2 \rangle = (r/r_0^h)^{\gamma_h}, \quad (15)$$

where  $\langle \dots \rangle$  denotes the expected value,  $r = |\mathbf{r}|$  is the length of a horizontal offset vector  $\mathbf{r}$ ,  $r_0^h$  is a measure of the scale size of phase fluctuations and  $\gamma_h$  is a power-law slope. Both  $r_0^h$  and  $\gamma_h$  are fixed parameters per layer that need to be specified by the user. This expression does not yet include a zenith angle dependence. For a finite number of IPPs  $\mathbf{p}_{ik}^h$  per layer and given values for  $r_0^h$  and  $\gamma_h$ , we can construct a structure matrix  $\mathbf{D}_{\phi\phi}^h$  with elements

$$\mathbf{D}_{\phi\phi}^h[a, b] = D_{\phi\phi}^h(|\mathbf{p}_a^h - \mathbf{p}_b^h|), \quad (16)$$

where  $a, b \in \{(i, k)\}$  are antenna-source pair indices. Appendix A of Intema et al. 2009 contains a recipe to translate the phase structure matrix  $\mathbf{D}_{\phi\phi}^h$  into a phase covariance matrix  $\mathbf{C}_{\phi\phi}^h$  with elements

$$\mathbf{C}_{\phi\phi}^h[a, b] = C_{\phi\phi}^h(|\mathbf{p}_a^h - \mathbf{p}_b^h|), \quad (17)$$

with the phase covariance function  $C_{\phi\phi}^h(r)$  given by

$$C_{\phi\phi}^h(r) = \langle \phi^h(\mathbf{p}^h) \phi^h(\mathbf{p}^h + \mathbf{r}) \rangle. \quad (18)$$

Under the assumption of independence between layers, the integrated phase covariance matrix  $\mathbf{C}_{\phi\phi}$  of radio waves that travel through the multiple layers at zero zenith angle

is a combination of the covariance matrices  $\mathbf{C}_{\phi\phi}^h$  of individual independent layers

$$\mathbf{C}_{\phi\phi} = \sum_h w_h^2 \mathbf{A}^h \mathbf{C}_{\phi\phi}^h \mathbf{A}^h \equiv \sum_h w_h^2 \hat{\mathbf{C}}_{\phi\phi}^h. \quad (19)$$

Here, the zenith angle dependence is included by modifying the elements of each covariance matrix  $\mathbf{C}_{\phi\phi}^h$  before summation in Equation 19:

$$\hat{\mathbf{C}}_{\phi\phi}^h[a, b] = \frac{\mathbf{C}_{\phi\phi}^h[a, b]}{\cos(\zeta_a^h) \cos(\zeta_b^h)} \quad (20)$$

Derivation of the (truncated) set of dominant base vectors  $\tilde{\mathbf{U}}$  for describing the multi-layer model is done by discrete Karhunen-Loève (KL) transform of the multi-layer covariance matrix  $\mathbf{C}_{\phi\phi}$ . Similar to the single-layer model, the discrete phase vector  $\Phi$  along individual LoS's is represented by a linear combination of the dominant base vectors

$$\Phi = \tilde{\mathbf{U}}\mathbf{q}, \quad (21)$$

The model parameter vector  $\mathbf{q}$  is determined by NLLS minimalization of the difference between the model phase vector  $\Phi$  and the phase solutions obtained by peeling bright sources in the target field-of-view (FoV). Interpolation of the phase model to arbitrary viewing directions is done by Kriging interpolation, using Equation 19 to calculate the covariance matrix  $\mathbf{C}_{\hat{\phi}\phi}$  between the LoS's towards the peeling sources and the LoS's towards the sources  $\hat{k}$  of interest

$$\hat{\Phi} = \mathbf{C}_{\hat{\phi}\phi} \mathbf{C}_{\phi\phi}^{-1} \Phi. \quad (22)$$

Appendix A contains a recipe for reconstructing the structure of individual layers through interpolation.

### 3.2. Instrumental Phase Drift Estimation

One of the main assumptions in our ionospheric calibration scheme is that instrumental and ionospheric phase errors are separable on their spatial and temporal behaviour. Antenna-based instrumental phase errors are assumed to be constant with time and viewing direction, while ionospheric phase errors are assumed to vary with both. For extended (5–10 hour) low-frequency radio observations with both VLA and GMRT, we have noticed significant ( $> 20$  degrees) phase drifts of one or more antennas over the observing run that appear to originate from the instrument rather than ionosphere. We have also identified distinct phase offsets for some antennas, which are probably the result of inaccuracies in the initial estimation of the instrumental phase offsets (Intema et al. 2009, Section 3.1). To improve the modeling accuracy of ionospheric phase errors, these drifts and offsets need to be removed.

In SPAM we have used the direction-independence as an additional constraint to estimate residual instrumental phase offsets per visibility time interval  $n$ . Under the assumptions that (i) the residual instrumental phase offsets for the majority of antennas are relatively small, and (ii) SPAM fits reasonably accurate phase models to the peeling phase corrections  $\phi^{\text{cal}}$ , the residual instrumental phase offset on a particular antenna can be estimated by calculating the mean offset between the phase model and the peeling

phase solutions of the antenna towards multiple calibrator sources:

$$\Delta\phi_{in}^{\text{instr}} \approx \langle (\phi_{ikn}^{\text{cal}} - \phi_{ikn}^{\text{ion}}) \bmod 2\pi - \langle (\phi_{jkn}^{\text{cal}} - \phi_{jkn}^{\text{ion}}) \bmod 2\pi \rangle_{j \neq i} \rangle_k. \quad (23)$$

The average  $\langle \dots \rangle_{j \neq i}$  estimates and removes the offset between the model and the peeling phase correction towards each calibrator source.

The estimated residual instrumental phase offset for single antennas as a function of time (Figure 3) generally shows a scatter of points centered around a slowly changing phase component. Interpreting these as noise and instrumental residual phase, respectively, we apply a median window filter with a width of 1–2 hours to extract the slowly changing component. If at least one antenna shows a significant (say  $\gtrsim 10$  degrees) residual instrumental phase offset during the observing run, the extracted, the slowly varying instrumental phases are corrected for in both the visibility data set and the previously obtained phase measurements to which the phase model was fitted. Repeating the model fitting to the corrected phase measurements can lead to significant reductions in the RMS phase residuals (Section 4.3).

## 4. Applications

To test the effect of SPAM ionospheric calibration with a multi-layer ionospheric model, we apply this technique to archival VLA 74 MHz observations in the A-configuration, which is the largest low-frequency array presently available. We compare performance of this technique (labelled SPAM3D here) against SPAM calibration with a single-layer model (SPAM2D) by analyzing the resulting images. The data reduction and results of these test cases are described in detail. Because our data reduction procedure differs from other approaches (e.g. Lazio, Kassim, & Perley (2005), this description may serve as a template for other data reductions using SPAM.

### 4.1. Data Selection, Preparation and Processing

For our tests we chose to re-process the visibility data sets that were used by Cohen et al. (2004) to produce the deepest high-resolution 74 MHz maps to date. These observations are extended exposures with the VLA-A of two target fields near the Galactic Northpole that partially overlap, recorded during a single observing session. Although the targeted galaxies for these observations, NGC 4565 and NGC 4631, were not detected, both fields are large and deep enough to allow for  $\sim 1000$  source detections at the  $5\sigma$  level in total. Cohen et al. qualify the ionospheric conditions as ‘favourable’.

The original data processing included a phase calibration of the target field against a model derived from the NVSS source catalog (Condon et al. 1994; 1998) before applying field-based calibration (Cotton et al. 2004). Adding this initial phase calibration step is known to yield better quality images in some cases, even when it undermines the assumption of a constant instrumental phase in field-based calibration. The images were generated with robust weighting (Briggs 1995), using a circular  $25''$  restoring beam. The background noise level in the center of the image is estimated at  $35 \text{ mJy beam}^{-1}$ . The resulting images show

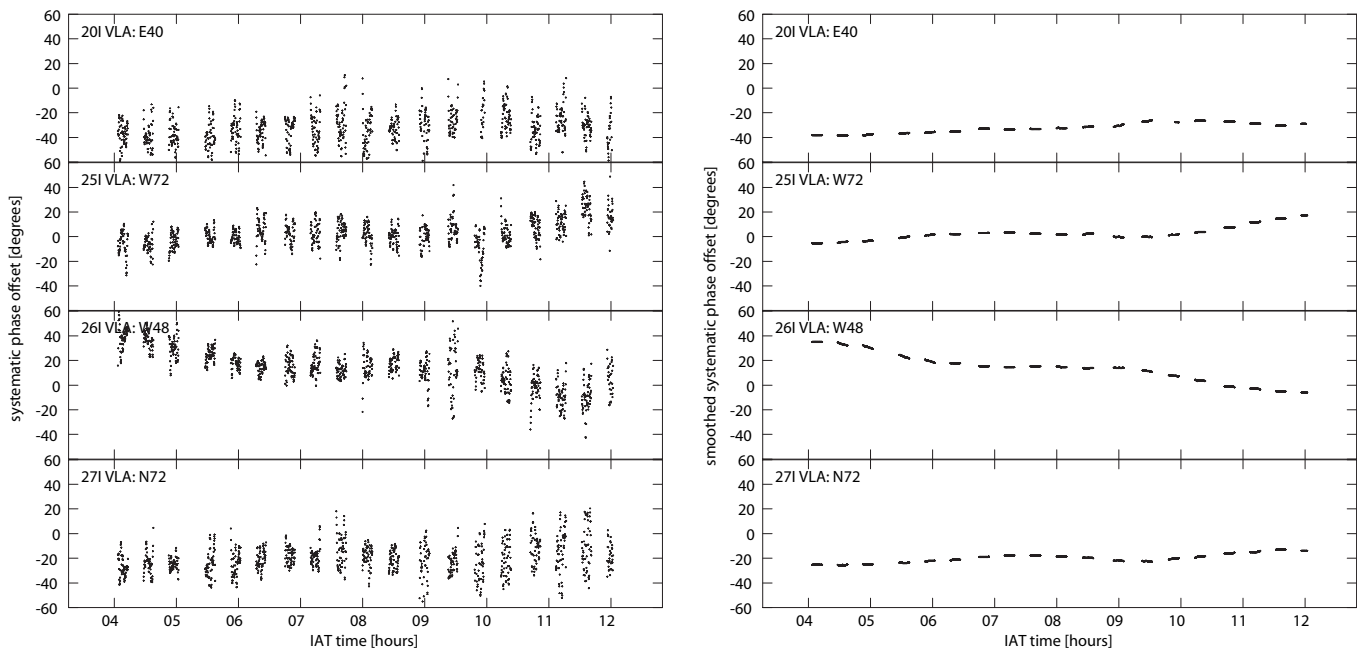


Figure 3: Plots of the systematic phase offsets after model fitting of four selected antennas as a function of time, using the method described in Section 3.2. These estimates were derived from the observation on NGC 4565 as presented in Section 4. *Left*: The phase offsets for individual visibility time stamps are noisy, but the underlying trends are clearly visible. *Right*: Median window filtering over sufficient long time scales isolates the trend from the noise. VLA antennas E40 and N72 have distinct constant offsets that probably resulted from a poor initial instrumental phase calibration. The systematic phase offsets for antennas W72 and W48 appear to be phase drifts that originate from the instrument itself. These observed trends are independently derived and confirmed from the alternated observation on NGC 4631.

signs of residual calibration errors, because there are ring-like and radial patterns present in the image background near bright sources.

Because we prefer to keep the assumption of constant instrumental phases intact (at least, initially), we decided not to use the partially reduced data sets from Cohen et al., but to extract the raw data from the VLA archive and redo the data reduction.

#### 4.2. Data Reduction

During a single 8.5 hour night observing session in 1998 on March 6–7 (03:46–12:11 IAT = 20:46–05:11 MST at the VLA), the targets NGC 4565 (RA  $12^{\text{h}}36^{\text{m}}23.705^{\text{s}}$ , DEC  $+26^{\circ}13'29.81''$ , J2000. epoch throughout) and NGC 4631 (RA  $12^{\text{h}}40^{\text{m}}56.379^{\text{s}}$ , DEC  $+32^{\circ}31'33.09''$ ) were observed with the VLA in A-configuration for 159 minutes each in alternating blocks of  $\sim 10$  minutes. The calibrator Cyg A was observed once for 3.5 minutes at the end of the observing run. The data was recorded at a 10 second time resolution in two polarizations (RR and LL) in the 4P dual frequency mode (74 and 330 MHz), using 63 channels of 24.4 KHz each to cover a 1.54 MHz bandwidth centered at 73.8 MHz.

The resulting, publicly available visibility data set (project code AE119) was extracted from the VLA archive<sup>1</sup>. The full data set was loaded into NRAO’s Astronomical Image Processing Software (AIPS; Bridle & Greisen 1994) package for reduction, using both AIPS tasks and special-

ized routines in the SPAM package (Intema et al. 2009). After discarding all but the 74 MHz data for Cyg A and the two targets, the uvw-coordinates were converted from epoch B1950 to J2000. For convenience, we discuss the further data reduction in terms of one target field, although this actually applies to both target fields.

##### 4.2.1. Instrumental Calibration

The Cyg A data was manually flagged for radio frequency interference (RFI) and bad baselines based on excessive visibility amplitudes. To remove ionospheric phase errors towards the calibrator, a small subset of central frequency channels was used to calibrate the antenna-based gain phases against a Cyg A model<sup>2</sup> on the visibility time resolution. Normalized bandpass corrections were determined using the same data and model while temporarily applying the phase calibration. Both the phase corrections and bandpass corrections were applied while calibrating the antenna-based gain amplitudes against the model, using all frequency channels. The time-constant amplitude and bandpass corrections were applied to Cyg A and the target field. Next, the target field data was manually inspected per baseline to identify and flag excessive visibility amplitudes (mostly RFI).

To remove the constant phase offset between RR and LL polarization, a second phase calibration of Cyg A against the model was done at the visibility time resolution us-

<sup>1</sup> <https://archive.nrao.edu/archive/archiveproject.jsp>

<sup>2</sup> Obtained from <http://lwa.nrl.navy.mil/tutorial> and converted from epoch B1950 to J2000.

Target field diameter	14°9
Pixel size	5.7''
Weighting	robust <sup>a</sup>
Wide-field imaging	polyhedron (facet-based) <sup>b</sup>
Deconvolution	Cotton-Schwab CLEAN <sup>c</sup>
Number of initial facets	475
Facet diameter	0°81
Facet separation	0°67

<sup>a</sup> Briggs 1995

<sup>b</sup> Perley 1989; Cornwell & Perley 1992

<sup>c</sup> Schwab 1984; Cotton 1999;  
Cornwell, Braun & Briggs 1999

Table 2: Overview of imaging parameters for both target fields (NGC 4565 and NGC 4631).

ing the full band. The phase corrections for both polarizations were subtracted (RR-LL) and time-averaged per antenna. These averages were applied to the LL polarization of Cyg A and the target field, after which the RR and LL visibilities were combined into stokes I. To reduce storage and processing, each three frequency channels were averaged together, resulting in 21 frequency channels of 73.2 KHz each.

To remove the antenna-based instrumental phase offsets, a third phase calibration of Cyg A against the model was done at the visibility time resolution. The phase corrections were filtered to separate instrumental from ionospheric phase contributions, by fitting simultaneously for time-constant offsets and time-variant spatial gradients over the array (Intema et al. 2009, Section 3.1). The time-constant instrumental phase offsets were applied to the target field. At this point, the target field data is assumed to be instrumentally calibrated, except for an unknown spatial phase gradient over the array.

#### 4.2.2. Initial Target Field Calibration and Imaging

After instrumental calibration, the astrometry for the target field was approximately restored by phase calibrating against a source model (30 second time resolution). The source model was derived by selecting from the VLSS catalog all sources within a primary beam radius from the pointing center, scaling their absolute fluxes to apparent fluxes by multiplication with an axisymmetric primary beam pattern (e.g., Lazio, Kassim & Perley 2005), and converting the 30 apparently brightest sources into a point source model. The calibration phase corrections were applied during the first imaging of the primary beam area (Table 2), followed by several rounds of phase-only self-calibration. Because it is crucial to keep the instrumental calibration intact, the calibration phase corrections were stored in tables and temporarily applied while imaging (instead of being applied directly). Per antenna, time ranges that showed excessive phase calibration corrections were flagged.

The VLA antennas are sensitive to flux coming from directions far outside the primary beam, mainly because of large sidelobes due to a relatively small antenna diameter (25 meter is just over 6 wavelengths at 74 MHz), and because scattering of waves of the primary focus support legs (Kassim et al. 2007). Because the dirty beam sidelobe pattern scales radially with wavelength, bright outlier sources

can induce noticeable sidelobe patterns in the target field image at this frequency. This potential problem is addressed in two steps: (i) subtraction of bright sources within a few primary beam radii of the pointing center, and (ii) subtraction of extremely bright sources at (possibly) very large angular distances from the pointing center.

For the first step, the final imaging round in the phase self-calibration loop on the target field included  $\sim 30$  additional facets centered at the positions of very bright VLSS sources outside the primary beam area, up to four times the primary beam radius (except for Vir A, which is processed in the second step). If detected (typically 5–10 sources), the CLEAN models of these outlier sources were subtracted from the visibility data while temporarily applying the self-calibration phase corrections. None of the detected sources were bright enough to be peeled.

For the second step of outlier removal, the updated source models were subtracted from the flagged target field data. The residual data was used to image 9 additional facets at large angular distance from the target field, centered on the Sun and 8 extremely bright sources, namely Cyg A, Cas A, Tau A, Vir A, Ori A, Sgr A, 3C 123 and 3C 10. For imaging and deconvolution of each source, we used the visibility time ranges during the observing run for which the source was above the local VLA horizon (assuming a locally flat Earth and ignoring source refraction). For both target fields, only Cyg A and Vir A were detected, at 87 and 14 degrees distance from NGC 4565, and 82 and 20 degrees from NGC 4631, respectively. Especially Vir A generated significant sidelobe noise in the NGC 4565 image (Figure 4). Both Cyg A and Vir A were peeled and subtracted from the target field visibility data, again taking into account the time ranges for which these sources were above the horizon.

The resulting target field data, with the outlier sources subtracted, was phase (self-)calibrated and imaged, after which the source model was subtracted from the visibility data. This residual data was inspected per baseline to flag visibilities with excessive amplitudes. Time-frequency blocks that had a large fraction of visibilities flagged were flagged completely. The resulting flagging tables were transferred and applied to the (non-subtracted) target field data, followed by re-imaging.

#### 4.3. Ionospheric Calibration and Imaging

To suppress the direction-dependent calibration errors due to ionospheric phase rotations, we applied SPAM calibration to the target field data, following the recipe in Intema et al. (2009). Each target field data set was processed for two calibration cycles using the single-layer model (SPAM2D). The second cycle was then repeated using the multi-layer model (SPAM3D) on the same (model independent) calibration data. For SPAM2D we used the same model settings as in the previous test cases described in Intema et al., using a screen height  $h = 200$  km and a phase structure function power law exponent  $\gamma = 5/3$ . For SPAM3D, we used a multi-layer model with the dominant layer at  $h = 200$  km and two additional layers to add a simple vertical structure (see Table 3), using  $\gamma = 5/3$  for all layers.

The data processing steps in Section 4.2.2 yielded per target field (i) an instrumentally calibrated, flagged visibility data set with outlier sources suppressed, (ii) a table

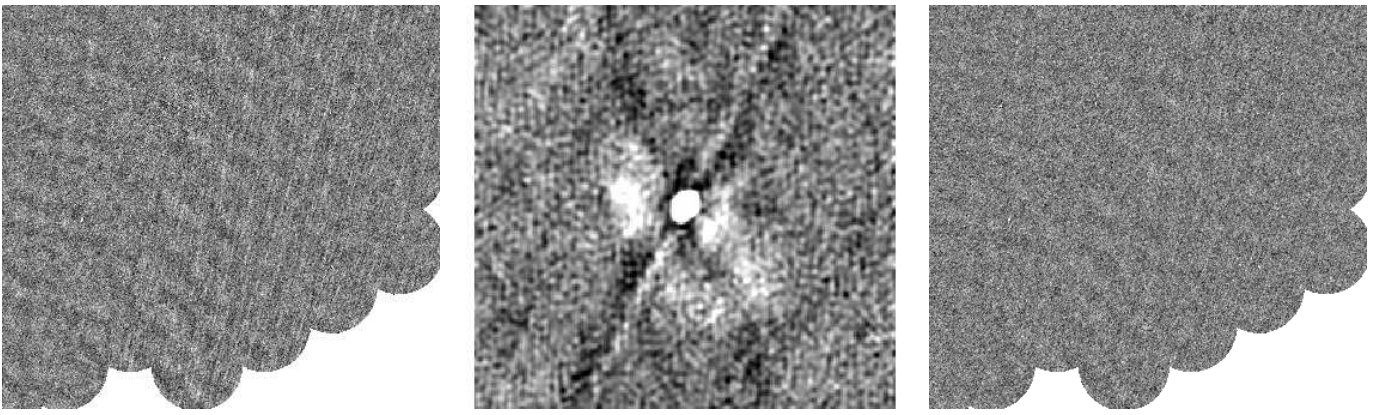


Figure 4: Example of the effect of bright outlier removal. *Left*: South-west boundary of the NGC 4565 field before outlier removal. This image contains considerable background structure (near-vertical striping) due to the presence of Vir A. *Middle*: Image of Vir A as derived from peeling, imaged at 14 degrees from the field center. *Right*: Same as left but with Vir A subtracted, which significantly reduces the background structure.

with self-calibration phase corrections, (iii) a deconvolved target field image and (iv) a target field source model. This data was used as an initial estimate to start the SPAM calibration cycle, consisting of the following steps:

1. Subtract the source model from the visibility data while applying the phase calibration. Peel apparently bright sources.
2. Fit an ionospheric phase screen model to the peeling solutions. Remove systematic (instrumental) phase drifts.
3. Apply the model phases during re-imaging of the target field.

Compared to Intema et al., the cycle is changed by adding to step 2 an instrumental phase drift estimation as described in Section 3.2.

The peeling step typically yielded  $\sim 15$  sources for which direction-dependent phase calibration corrections could be obtained. The SPAM model was fitted to the peeling phase corrections using the arbitrary number of 20 free parameters for all rounds of processing. The instrumental phase drift correction was mainly effective in the first SPAM cycle (see Figure 3 for an example), reducing the typical RMS residual phase from  $\sim 40$  to  $\sim 30$  degrees. After each modeling step, visibility time stamps that had a RMS residual phase higher than 40 degrees were discarded (Figure 5). In two calibration cycles, this removed a substantial ( $\sim 30$  percent) fraction of the data, mainly during the final 3 hours of the observing run. For both fields, the mean RMS residual phase for SPAM3D is slightly lower than for SPAM2D (Table 3).

#### 4.4. Output Image Comparison

Because there is no information available on the true ionosphere induced phase errors, we analyze the output images from the SPAM2D and SPAM3D calibration strategies to determine the relative performance. It is not our goal to repeat the in-depth comparison against field-based calibration (for this, see Intema et al. 2009). However, we do perform some basic sanity checks against one of the two target field images from Cohen et al. (2004), namely NGC 4565.

Field name	NGC 4565	NGC 4631
Peeling sources	17	13
Model layer heights (weights):		
SPAM2D:	200 km (1.00)	200 km (1.00)
SPAM3D:	100 km (0.25)	100 km (0.25)
	200 km (0.50)	200 km (0.50)
	400 km (0.25)	400 km (0.25)
RMS residual phase [degrees]:		
SPAM2D	$30.8 \pm 3.6$	$27.66 \pm 4.79$
SPAM3D	$30.1 \pm 3.6$	$27.03 \pm 4.71$
Total flagged data fraction:		
SPAM2D	0.33	0.25
SPAM3D	0.32	0.25

Table 3: Overview of the SPAM processing parameters for both target fields (NGC 4565 and NGC 4631).

We label this as field-based calibration (FBC), but in reality it is a (possibly sub-optimal) combination of field-based calibration after applying a time-variable phase-calibration.

Residual ionospheric phase errors can generate several direction-dependent types of image artefacts. Because the images are generated from visibilities measured over an extended observing session, all time-varying residual phase errors are accumulated into time-averaged artefacts. Both image background and source properties are inspected for evidence of these artefacts. For convenience, none of the analyzed images have been corrected for primary beam attenuation, so the background noise is approximately flat.

A non-zero mean phase gradient over the array towards a source will cause an apparent position shift. Any non-zero mean higher order phase structure causes a deformation of the source. Both a zero-mean time variable phase gradient and higher order phase effects cause smearing and deformation of the source image, and consequently a reduction of the source peak flux (see Cotton & Condon 2002 for an example). In the presence of time-varying residual

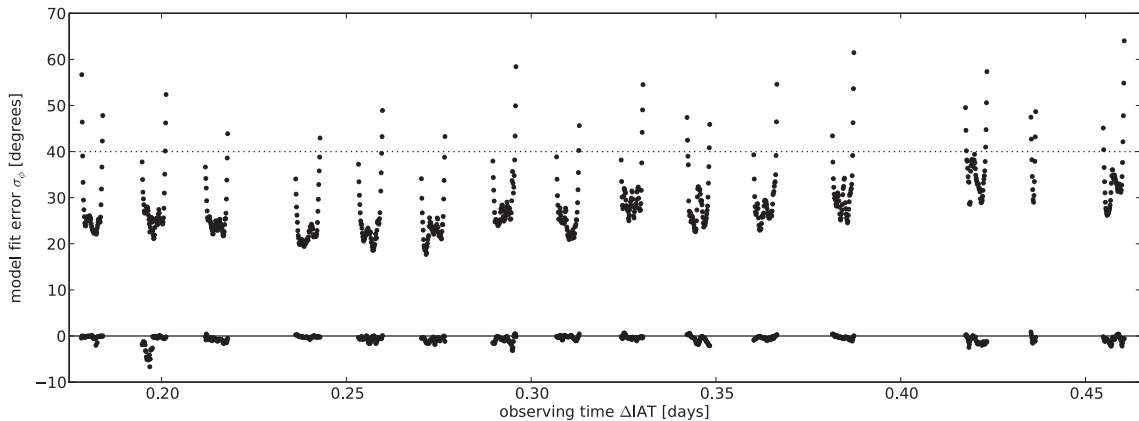


Figure 5: Example plot of the RMS residual phase as a function of visibility time stamp for the SPAM3D model fit on the peeling solutions of the NGC 4631 field. The phase residuals increase at the edge of each scan due to extrapolation inaccuracies of the peeling solutions. All time stamps with phase residuals larger than 40 degrees (dotted line) were discarded. The points near zero degrees (solid line) are the difference between the SPAM3D and SPAM2D RMS phase residuals (SPAM3D-SPAM2D).

phase errors, the source model subtraction during CLEAN deconvolution is incomplete because the average, apparent source model from the output image is distorted, and because the visibilities on individual time stamps deviate from the model visibilities due to the phase errors. Therefore, part of the image background noise level consists of residual sidelobes. The local sidelobe noise increases with both the RMS phase error and the local source flux. We use both the source peak fluxes, source peak positions and the background noise for our analysis.

When measured over a large image area, the mean sidelobe noise depends mainly on RMS phase error. For all relevant output images, the mean image noise  $\sigma$  was determined by fitting a Gaussian to the histogram of image pixel values from the inner quarter radius of the FoV where most apparent flux is (Table 4). For both fields, the noise levels for SPAM2D and SPAM3D are approximately equal. The SPAM noise levels are  $\sim 10$  percent lower than for FBC. Visual inspection of the images per field shows that there is very little difference in background structure between SPAM2D and SPAM3D. The FBC image shows relatively more traces of deconvolution errors near bright sources.

To allow for comparison of source properties, we applied the source extraction tool BDSM (Mohan et al. 2008) on all relevant images. BDSM performs a multiple 2-dimensional Gaussian fit on islands of adjacent pixels with amplitudes above a specified threshold based on the *local* image noise  $\sigma_L$  in the image. Multiple overlapping Gaussians are grouped together into single sources. We applied BDSM to all images, using the default extraction criteria (which includes that a source detection requires at least 4 adjacent pixel values above  $3\sigma_L$ , with at least one pixel value above  $5\sigma_L$ ).

Table 4 contains the number of sources cataloged by BDSM within a 6 degree radius from the field center, with the additional constraint that the peak flux is at least 5 times the mean background noise. Additionally, each catalog was cross-associated against the NVSS catalog (Condon et al. 1994, 1998), which has a lower resolution ( $45''$ ) but

also a much lower detection limit (at least 5 times lower for an average spectral index of  $-0.8$ ). Table 4 lists the number of sources (and fractions) that have an NVSS counterpart within  $60''$ . This limit gives sufficient room to resolve resolution issues (e.g. single source in NVSS might be double in 74 MHz images) while introducing very few false associations (Cohen et al. 2007). For the SPAM methods, the association fractions are slightly higher for the NGC 4631 field, which makes the total number of associations for both fields roughly equal. FBC has a slightly lower association fraction, which results in  $\sim 8$  percent less associated sources as compared to SPAM2D and SPAM3D. To minimize contamination with fake detections, we continue our analysis with sources that have an NVSS counterpart, thereby risking the loss of an incidental ultra-steep spectrum source.

To compare source properties from the different calibration techniques, the available catalogs for each field are individually cross-associated with a  $60''$  search radius. The peak fluxes of associated sources are plotted in Figure 6. We use peak fluxes rather than integrated fluxes because of the larger uncertainties in the integrated flux determination, and because a significant fraction of sources is unresolved at  $25''$  resolution. For each field, there is a tight match between source peak fluxes from the different calibration methods. For sources that have peak fluxes  $> 10\sigma$  in both catalogs, the mean peak flux ratio lies within 2 percent of unity. The relatively high association fraction and relatively tight peak flux correlation between SPAM2D and SPAM3D is expected to be strongly influenced by the common SPAM data reduction steps.

Despite the low resolution ( $45''$ ) of the NVSS, the RMS position error for NVSS sources  $> 15$  mJy is better than  $1''$ . The astrometric accuracy of extracted sources in the two 74 MHz target field images is expected to be worse, as they are likely to be dominated by systematic residual phase gradients after ionospheric calibration (e.g., see Intema et al. 2009). We estimate the astrometric errors in the target fields by comparing the peak positions of a subset of  $> 300$  compact sources (gaussian width  $< 32.5''$ ) against the peak

Field name	NGC 4565	NGC 4631
Mean background noise $\sigma$ [mJy beam <sup>-1</sup> ]:		
FBC	33.1	–
SPAM2D	29.6	32.6
SPAM3D	30.3	32.5
Number of sources within a 6 degree radius with a peak fluxes $> 5\sigma$ :		
FBC	559	–
SPAM2D	605	572
SPAM3D	584	582
$5\sigma$ source count (and fraction) with an NVSS counterpart within $60''$ :		
FBC	511 (0.916)	–
SPAM2D	568 (0.939)	549 (0.961)
SPAM3D	550 (0.942)	556 (0.957)

Table 4: Overview of results from calibrating and imaging two test fields with field-based calibration (FBC) applied, single-layer SPAM (SPAM2D) calibration applied and multi-layer SPAM (SPAM3D) applied.

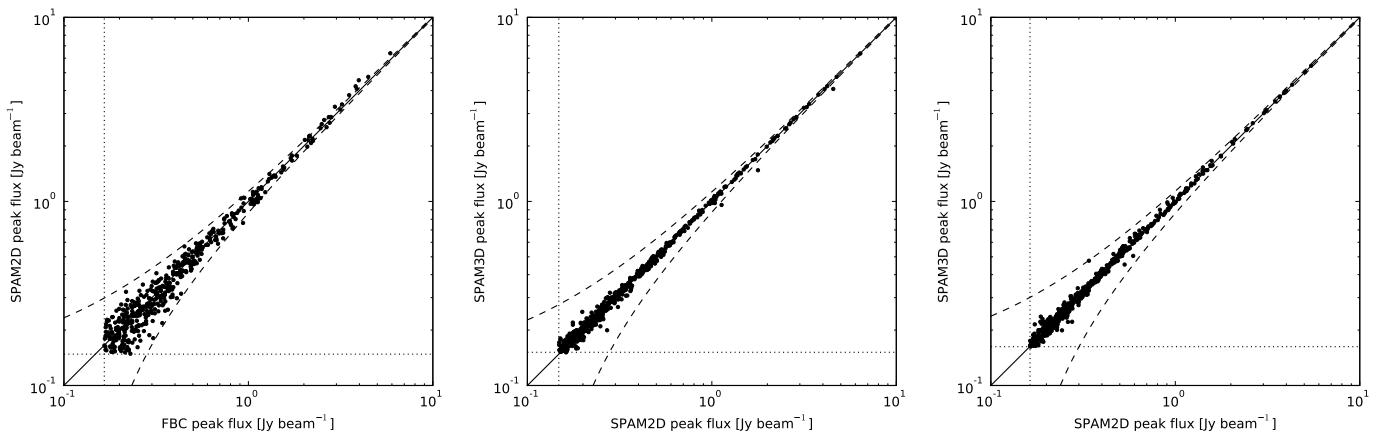


Figure 6: Peak flux comparisons in the NGC 4565 and NGC4631 fields *Left*: Peak flux comparison for 474 sources detected in both the FBC and SPAM2D images of the NGC 4565 field. The straight diagonal line represents equality, the dashed lines represent  $3\sigma_C$  deviations (where  $\sigma_C$  is the combined noise level from both images), and the dotted lines indicate the  $5\sigma$  detection limit. The peak flux comparison of 472 sources between FBC and SPAM3D for the same field (not plotted here) is very similar. *Middle*: Same for 537 sources in the SPAM2D and SPAM3D images of the NGC 4565 field. *Right*: Same for 539 sources in the SPAM2D and SPAM3D images of the NGC 4631 field.

positions of close NVSS sources (within  $10''$  to minimize resolution mismatches). Note that a changing spectral index across a source may add to the observed position difference, but this effect is equal for both the calibration methods (SPAM2D and SPAM3D) under examination. The position differences for both fields and both calibration methods are plotted in Figure 7.

For both target fields and both SPAM versions, the position offsets are scattered around a mean that is systematically offset from zero by  $\lesssim 1''$  in roughly the same direction. Because the astrometry for the whole field depends on the accuracy of the assumed (NVSS) positions of the  $\sim 15$  peeled calibrators, it is most likely that a non-zero mean position error in the assumed calibrator positions causes the observed systematic offset, which is (by coincidence) similar in amplitude and direction for both fields. We continue by removing the systematic offset from all catalog positions.

For the NGC 4565 field the measured RMS position offsets around the zero mean are  $3.44''$  and  $3.27''$  for SPAM2D and SPAM3D, respectively, and for the NGC 4631 field the measured RMS position offsets are  $3.24''$  and  $2.96''$ , respectively. Removing the intrinsic  $< 1''$  RMS position error in NVSS would lower these values by  $0.17''$  at most, but this correction has little consequence for our performance comparison. By differencing the RMS position offsets in quadrature, we estimate that using SPAM3D instead of SPAM2D improved the overall RMS astrometric accuracy by  $1.31''$  and  $1.07''$  for the NGC 4565 and NGC 4631 fields, respectively.

## 5. Discussion and Conclusions

We have extended the ionospheric phase calibration method SPAM by Intema et al. (2009) with a multi-layer ionosphere model and an instrumental phase drift esti-

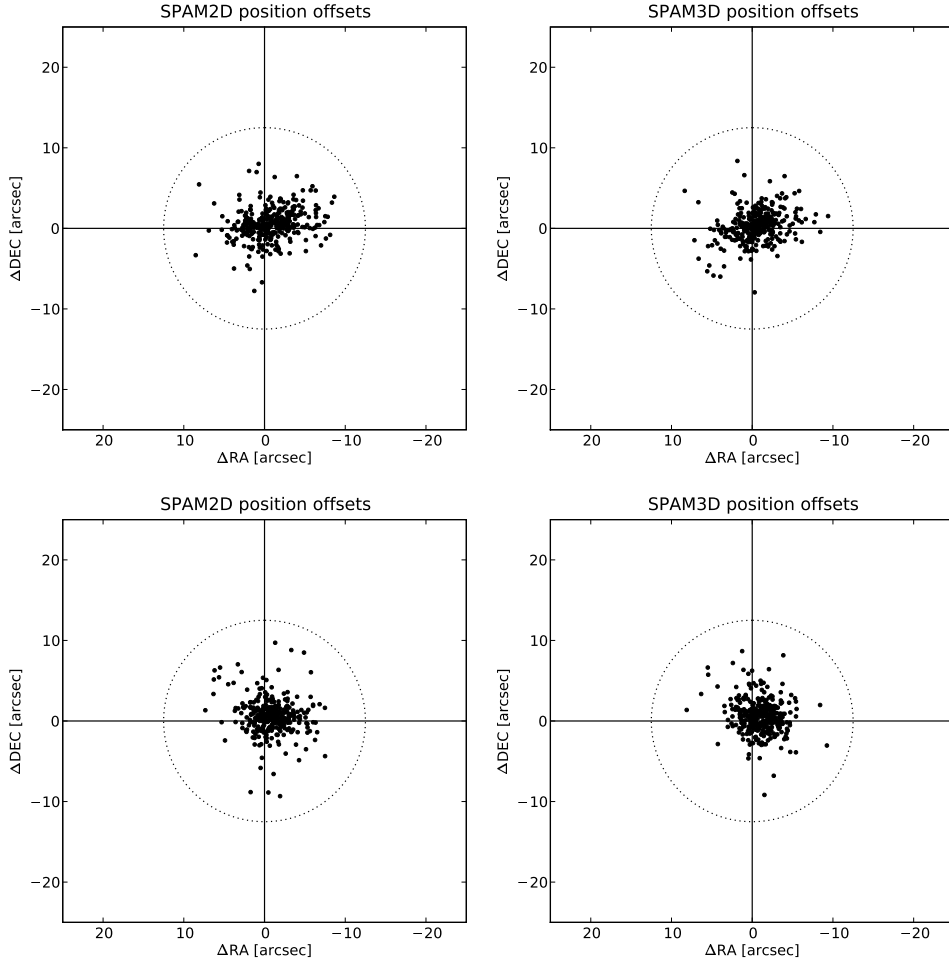


Figure 7: Position offsets of a subset of compact sources in the NGC 4565 field (*top row*) and NGC 4631 field (*bottom row*) as measured in the SPAM2D images (*left column*) and SPAM3D images (*right column*), using the NVSS catalog as a reference. The dotted line marks the size of the  $25''$  restoring beam.

mator, in an attempt to improve the calibration accuracy of wide-field low frequency radio interferometric observations. The SPAM method has been successfully tested on simultaneous, extended 74 MHz VLA observations of two fields in the largest A-configuration under quiet ionospheric conditions. From this test case we draw the following conclusions:

(i) Using a multi-layer ionosphere model is at least as accurate as using a single-layer model, but probably more accurate. Application of the multi-layer model resulted in a small improvement in the overall astrometric accuracy as compared to the single-layer model, while no noticeable changes are observed in the background noise or source peak fluxes. Global distortions in the astrometry are induced by residual phase gradients that vary across the FoV. For a single-layer model, we estimated that the presence of a 3-dimensional bulk ionosphere will cause systematic phase gradient errors. Although not conclusive, an improved representation of the large-scale 3-dimensional ionosphere by the multi-layer model can explain the improvement in astrometry, while the other image characteristics should remain the same. This improved representation may also be reflected in the small reduction of the RMS phase residual after model fitting, which can indicate a better consistency between the astrometry of

the calibrators and the multi-layer model as compared to the single-layer model.

(ii) The phase drift estimator was successful in detecting and removing several large antenna-based phase offsets and drifts from the visibility data. This significantly reduced the RMS residual phase after SPAM model fitting by  $\sim 25$  percent on average. The phase offsets are probably the result of an inaccurate instrumental phase estimation from a relatively short calibrator observation. The phase drifts (up to 40 degrees over 8 hours for one antenna) do not have a clear cause. Because the data reduction does not apply time-variable phase corrections before this estimator, and because the same phase drifts are observed in both target field data sets, we exclude our data processing as a possible cause for the phase drifts. The ionosphere itself is an unlikely candidate, because of the persistent nature of the phase deviations and the absence of the same phase structure on neighbouring antennas. Mechanical deformation or communication delay changes are unlikely, because the VLA is known to be phase stable on much higher observing frequencies (also, a 40 degree phase change at 74 MHz corresponds to a significant path length difference of  $\sim 45$  cm). Possibly, the phase drifts are induced in 74 MHz-specific receiver hardware at some antennas.

(iii) Our full data reduction, including SPAM ionospheric calibration, generated images in which the flux scale is well matched to an earlier, independent data reduction by Cohen et al. (2004). There is no noticeable improvement in the peak fluxes, but the mean background noise level in the central beam area has lowered by  $\sim 10$  percent to  $\sim 30$  mJy beam $^{-1}$ . The improved suppression of sidelobes appears to be the main reason, which indicates a modest improvement in phase calibration accuracy.

To further explore the performance, robustness and limitations of the SPAM method, we will continue to process data sets obtained with different existing low-frequency arrays under different ionospheric conditions. We also investigate possibilities to improve the calibration accuracy further, like including time evolution in the ionosphere model. Developments for testing SPAM in a simulated environment are currently in progress.

*Acknowledgements.* The authors would like to thank Rudolf Le Poole, Reinout van Weeren, Niruj Mohan, Sridharan Rengaswamy, James Anderson, Ger de Bruyn, Jan Noordam, Maaijke Mevius, Juan Uson, Cathyn Mitchell, Paul Spencer, Ian McCrea and Hans van der Marel for useful discussions. HTI acknowledges a grant from the Netherlands Research School for Astronomy (NOVA). SvdT acknowledges NWO-STW grant number DTC.5893.

## References

- Bilitza, D., 2001, ‘International Reference Ionosphere 2000’, Radio Science, 36, 2
- Blanch, J., Walter, T. & Enge, P., 2004, Proceedings of the 2004 National Technical Meeting of the Institute of Navigation, San Diego, California
- Bridle, A.H. & Greisen, E.W., 1994, AIPS Memo 87
- Briggs, D.S., 1995, PhD Thesis, New Mexico Institute of Mining Technology, Socorro, New Mexico, USA
- Bust, G.S., & Mitchell, C.N., 2008, Rev. Geophys, 46, RG1003
- Cohen, A.S., et al., 2004, ApJS, 150, 417
- Cohen, A.S., et al., 2007, ApJ, 134, 1245
- Condon, J.J., et al., 1994, ASPC, 61, 155
- Condon, J.J., et al., 1998, AJ, 115, 1693
- Cornwell, T.J., and Perley, R.A., 1992, A&A, 261, 353
- Cornwell, T.J., Braun, R. & Briggs, D.S, 1999, ASPC, 180, 151
- Cotton, W.D., 1999, ASPC, 6, 233
- Cotton, W.D. & Condon, J.J., 2002, Proceedings of URSI General Assembly, paper 0944
- Cotton, W.D., et al., 2004, SPIE, 5489, 180
- Davies, K., 1990, ‘Ionospheric Radio’, Institution of Engineering and Technology, Stevenage, UK
- Esposito, S., 2005, Comptes Rendus Physique, 6, 1039
- Fuller-Rowell, T.J., et al., 2006, Radio Science, 41, RS6003
- Hardy, J.W., 1998, ‘Adaptive Optics for Astronomical Telescopes’, Oxford University Press, Oxford, UK
- Intema, H.T., 2009, arxiv:0904.3975, accepted for publication in A&A
- Kassim, N.E., et al., 2007, ApJS, 172, 686
- Lazio, T.J.W., Kassim, N.E. & Perley, R.A., 2005, ‘Low-Frequency Data Reduction at the VLA: A Tutorial for New Users’, version 1.13
- Marchetti, E., 2007, The Messenger 129 (ESO), 8
- Matheron, G., 1973, Advances in Applied Probability, 5, 439
- Mohan, N.R., 2008, ‘ANAAMIKA manual’, version 2.1, available online through [http://www.strw.leidenuniv.nl/~mohan/anaamika\\_manual.pdf](http://www.strw.leidenuniv.nl/~mohan/anaamika_manual.pdf)
- Noordam, J.E., 2004, SPIE, 5489, 817
- Pearson, T.J., & Readhead, A.C.S., 1984, ARA&A, 22, 97
- Perley, R.A., 1989, ASPC, 6, 259
- Roddier, F., 1981, Progress in Optics, 19, 283
- Schwab, F.R., 1984, AJ, 89, 1076
- Smith, D.A., et al., 2008, Radio Science, 43, RS6008
- Thompson, A.R., Moran, J.M. & Swenson, G.W., 2001, ‘Interferometry and Synthesis in Radio Astronomy’, Second Edition, Wiley, New York

van der Tol, S. & van der Veen, A.J., 2007, Proceedings of the IEEE International Symposium Signals, Circuits, Systems, Iasi, Romania

van Velthoven, P.F.J., 1990, PhD Thesis, Eindhoven University of Technology, Eindhoven, The Netherlands

## Appendix A: Reconstruction of Ionospheric Model Layers

This Section contains a recipe for estimating the phase structure of individual layers in a multi-layer ionosphere model as described in Section 3.1.

The model base vectors are derived by performing a Karhunen-Loève (KL) transform (singular value decomposition) on the total phase covariance matrix defined in Equation 19:

$$\mathbf{C}_{\phi\phi} = \mathbf{U}\mathbf{\Lambda}\mathbf{U}^T, \quad (\text{A.1})$$

where the columns of  $\mathbf{U}$  contain a set of orthonormal base vectors,  $\mathbf{U}^T$  is the transpose of  $\mathbf{U}$  and the diagonal matrix  $\mathbf{\Lambda}$  contains measures of the variance of the base vector coefficients. Equation 19 defines the total phase covariance matrix  $\mathbf{C}_{\phi\phi}$  as a weighted sum of the phase covariance matrices  $\hat{\mathbf{C}}_{\phi\phi}^h$  per layer. Performing a KL transform on individual layers gives:

$$\hat{\mathbf{C}}_{\phi\phi}^h = \mathbf{U}_h\mathbf{\Lambda}_h\mathbf{U}_h^T. \quad (\text{A.2})$$

The KL transform is a non-linear operation, i.e. the base vectors  $\mathbf{U}$  are not a weighted sum of the layer base vectors  $\mathbf{U}_h$ :

$$\mathbf{U}\mathbf{\Lambda}\mathbf{U}^T = \sum_h w_h^2 \mathbf{U}_h\mathbf{\Lambda}_h\mathbf{U}_h^T \Rightarrow \mathbf{U} \neq \sum_h w_h \mathbf{U}_h. \quad (\text{A.3})$$

This means that we cannot perform an exact reconstruction of individual phase screens in a multi-layer configuration, even when the model parameter vector  $q$  is fitted with infinite accuracy (Equation 21):

$$\mathbf{\Phi}^h \neq \mathbf{U}_h \mathbf{q}. \quad (\text{A.4})$$

An approximate reconstruction is possible by Kriging interpolation to the individual layers

$$\hat{\mathbf{\Phi}}^h = w_h \hat{\mathbf{C}}_{\phi\phi}^h \mathbf{C}_{\phi\phi}^{-1} \mathbf{\Phi}. \quad (\text{A.5})$$

From Equation 19 it follows that this approximation obeys Equation 14:

$$\sum_h w_h \hat{\mathbf{\Phi}}^h = \mathbf{\Phi}. \quad (\text{A.6})$$

This interpolation could be interpreted as ionospheric tomography: a reconstruction of the 3-dimensional phase structure of the ionosphere by means of reconstruction in layers. However, one must be cautious with the interpretation of the fitted semi-empirical model, which doesn’t necessarily correspond to reality.